




# On the long-term oxidation behaviour of homogeneous Ni–Fe–Cu alloys for CO<sub>2</sub>-free aluminium electrowinning applications at 800 °C

Thomas Jamieson<sup>1,2,\*</sup> , Daniel Apel<sup>3</sup>, Andrey Yasinskiy<sup>4,5</sup>, Roman Düssel<sup>5</sup>, Peer Decker<sup>5</sup>, Gudmundur Gunnarsson<sup>6</sup>, Kamaljeet Singh<sup>7,8</sup>, Jon Magnusson<sup>9</sup>, Bastian Adam<sup>2</sup>, Ralf Busch<sup>2</sup>, Bernd Friedrich<sup>4</sup>, and Isabella Gallino<sup>1,2</sup>

<sup>1</sup> Chair of Metallic Materials, Technical University Berlin, Ernst-Reuter-Platz 1, 10587 Berlin, Berlin, Germany

<sup>2</sup> Chair of Metallic Materials, Saarland University, Campus, 66123 Saarbrücken, Saarland, Germany

<sup>3</sup> BESSY II, Helmholtz Zentrum Berlin, Hahn Meitner Platz 1, 610101 Berlin, Berlin, Germany

<sup>4</sup> IME Process Metallurgy and Metal Recycling, Intzestraße 3, 52056 Aachen, North-Rhine Westphalia, Germany

<sup>5</sup> TRIMET Aluminium SE, Aluminiumallee 1, 45356 Essen, North-Rhine Westphalia, Germany

<sup>6</sup> IceTec, Arleynir 8, Reykjavik 112, Iceland

<sup>7</sup> Department of Engineering, Reykjavik University, Aluminiumallee 1, Reykjavik 102, Iceland

<sup>8</sup> Department of Materials Science and Engineering, NTNU, Aluminiumallee 1, Trondheim 7491, Norway

<sup>9</sup> Arctus Aluminium Ltd, Arleynir 8, Reykjavik 112, Iceland

**Received:** 9 July 2025

**Accepted:** 29 July 2025

© The Author(s), 2025

## ABSTRACT

The oxidation behaviour of homogeneous Ni<sub>29</sub>Fe<sub>56</sub>Cu<sub>15</sub> wt.%, Ni<sub>42</sub>Fe<sub>38</sub>Cu<sub>20</sub> wt.% and Ni<sub>60</sub>Fe<sub>30</sub>Cu<sub>10</sub> wt.% is investigated under 1 atm flux of high-purity O<sub>2</sub> gas—using thermogravimetry—with respect to application as oxygen-evolving anodes for aluminium electrolysis. Stable cubic oxidation behaviour was observed in Ni<sub>42</sub>Fe<sub>38</sub>Cu<sub>20</sub> wt.% and Ni<sub>60</sub>Fe<sub>30</sub>Cu<sub>10</sub> wt.% after 30 h and 264 h, respectively, with the former showing particular promise for electrowinning applications due to a tendency to form a well-adhered scale consisting of approximately 70% NiFe<sub>2</sub>O<sub>4</sub> by thickness, as measured from EDX line scans. NiO dominated the scale of Ni<sub>60</sub>Fe<sub>30</sub>Cu<sub>10</sub> wt.% up to 272 h, showing worse scale adhesion and prominent intergranular oxidation of iron. Partially blistered regions of the scale locally increased NiO/CuO formation in Ni<sub>42</sub>Fe<sub>38</sub>Cu<sub>20</sub> wt.%, evolved to become (Cu/Ni, Fe)O spinel oxides over time.

Handling Editor: Megumi Kawasaki.

Address correspondence to E-mail: t.jamieson@campus.tu-berlin.de

E-mail Addresses: daniel.apel@helmholtz-berlin.de; andrei.iasinskiy@trimet.de; Roman.Duessel@trimet.de; peer.decker@trimet.de; gudmundur@taeknisetur.is; kamaljeets@ru.is; jhm@arctus.is; bastian.adam@uni-saarland.de; r.busch@mx.uni-saarland.de; bfriedrich@ime-aachen.de; gallino@tu-berlin.de

<https://doi.org/10.1007/s10853-025-11313-7>

Published online: 09 September 2025

 Springer

Content courtesy of Springer Nature, terms of use apply. Rights reserved.

## Introduction

Since the turn of the millennium, aluminium production from raw earth materials has increased by 286% since the end of 2023, with demand in industry rising due to its superior mechanical properties [1]. The Hall–Heroult process, the contemporary industry standard, operates in molten cryolite ( $\text{Na}_3\text{AlF}_6$ ) at 960 °C, allowing the dissolution of alumina and the reduction of liquid aluminium at the cathode. A carbon anode is used and consumed over the operation of the cell, primarily producing  $\text{CO}_{2(g)}$  among other harmful greenhouse gases (GHGs) such as perfluorocarbons (PFCs). The general equation using carbon anodes can be written as follows  $2\text{Al}_2\text{O}_3(\text{sol}) + 3\text{C}(\text{s}) \rightarrow 4\text{Al}(\text{l}) + 3\text{CO}_2(\text{g})$ . Replacing the carbon component with a non-reactive anode, the equation changes to  $2\text{Al}_2\text{O}_3(\text{sol}) \rightarrow 4\text{Al}(\text{l}) + 3\text{O}_2(\text{g})$ . This equation shows how  $\text{CO}_2(\text{g})$  may be removed with the implementation of a non-consumable so-called inert alternative where the electrochemical process produces  $\text{O}_2$  gas instead. The removal of GHG production from the electrochemical process, as well as saving in energy due to a vertical anode–cathode configuration with a distance of around 2 cm which results in reduced ohmic drop in the electrolyte and improved thermal management [2], makes the development of such anodes extremely desirable within the aluminium industry. To date, no such suitable solution for inert anode material has been found. The aggressive conditions in the cell, specifically with respect to corrosion via the electrolyte and oxygen gas, make the design of a non-consumable anode especially challenging. As well as good corrosion resistance and limited solubility within the electrolyte, the anode must also be electrically conductive, possess good thermal shock resistance to inhibit cracking/mechanical failure and be suitable for scaling up to industry level on a cost and practicality basis. Ni–Fe–Cu alloys have received much attention over the past three decades, first being suggested as a candidate material in 1995 [3] in particular for its tendency to form a mixed oxide,  $\text{NiFe}_2\text{O}_4$ , which has a relatively low solubility in the electrolyte, good corrosion resistance and adequate conductivity [4, 5]. Cu facilitates the formation of  $\text{NiFe}_2\text{O}_4$  due to its tendency to outwardly diffuse causing an initial CuO layer to form on the surface. This provides early protection against the electrolyte and extensive oxidation, allowing time for NiO and  $\text{Fe}_2\text{O}_3$  to form and react in a Cu-depleted region underneath [6, 7].

Despite a two-phase microstructure upon casting that negatively affects corrosion properties, there is evidence to suggest a reduced miscibility gap and a large FCC single-phase region exists, reachable through an appropriate heat treatment [8].

In 2012, Gallino, Kassner and Busch [9] gave account of one such promising as-homogenised alloy  $\text{Ni}_{42}\text{Fe}_{38}\text{Cu}_{20}$  wt.%, with stable cell operation up to 500 h [10], that has spurred some recent electrochemical investigations [11–14]. The corrosion resistance of a metallic anode is significantly influenced by the stability of the oxide scale it forms on the surface against cracking, spalling and dissolution. The oxidation behaviour of several Ni–Fe–Cu alloys has been documented previously over short-medium term oxidation experiments, with the alloys generally following a parabolic rate law and the oxide structure varying as a function of alloy composition [7, 10, 15–18]. This study will instead aim to describe the oxidation mechanisms and phase formations occurring in three alloys within this reduced miscibility gap region,  $\text{Ni}_{29}\text{Fe}_{56}\text{Cu}_{15}$  wt.%,  $\text{Ni}_{60}\text{Fe}_{30}\text{Cu}_{10}$  wt.% and  $\text{Ni}_{42}\text{Fe}_{38}\text{Cu}_{20}$  wt.%. The compositions were chosen to investigate the change in oxidation mechanism over a wide composition space within the single-phase region. Longer oxidation experiments at 800 °C were performed—up to 300 h—in an attempt to analyse the oxide structure and its applicability in molten salt aluminium electrolysis.

## Experimental

### Sample preparation

Pre-alloys of each composition were produced in a custom-made laboratory arc-melter furnace under an inert argon atmosphere by using the following method. High-purity nickel, iron and copper ( $\geq 99.95$  wt.% purity) were appropriately weighed and alloyed by melting in a pre-cleaned vacuum-cycled ( $10^{-3}$  mbar) argon atmosphere. These pre-alloys were flipped and re-melted through four separate cycles to ensure full mixing of the constituent elements. The ingots were then cast into cylindrical rods of 7 mm in diameter and a length of 45 mm via induction melting in a ceramic crucible with an Indutherm MC15 tilt-caster, modified to cast into an actively water-cooled copper mould. Casting occurred under a vacuum-prepared ( $10^{-2}$  mbar) inert argon atmosphere. The homogenisation heat treatment used to transform

the as-cast two-phase dendritic microstructure into a single FCC phase was performed with a Nabertherm vertical furnace under vacuum-prepared conditions and an inert argon atmosphere. Annealing was performed for 12 h at 1100 °C, similarly to the procedure of [8, 10] with a heating rate of approximately 0.2 °C/s. The alloys were furnace cooled upon completion. An as-cast and annealed sample was polished and etched with the standard aqueous ferric chloride solution for metallographic analysis. Microstructure analysis to validate a full homogenisation treatment was performed firstly with an optical microscope.

For the oxidation study homogenised rods were cut into small discs, the entire surface ground with SiC 15 µm grain sandpaper and degreased ultrasonically in ethanol.

### Oxidation and analysis

The oxidation samples were each measured with a caliper—with dimensions in the range of 1 mm < h < 3 mm and  $\phi$ 7 mm—to determine the surface area. Samples were fluxed with high-purity dry O<sub>2</sub> throughout the entirety of their run at a rate of 50 ml/min, at 800 °C inside of a NETZSCH STA 449C Jupiter Differential Thermal Analyser in the thermogravimetric analyser (TGA) mode. Samples were heated from 25–800 °C at a rate of 0.215 °C/s. The mass gain (normalised by the surface area) was plotted as a function of the isothermal time for five separate oxidation studies; 5 h, 8 h, 18 h, 72 h and 300 h. 5-h, 8-h and 18-h isothermal studies were chosen to observe the oxide scale evolution at different points during the alloy's initial more rapid phase of oxidation. Baseline measurements were performed with an empty alumina crucible in identical conditions to the measurements and subtracted from the TGA signals to obtain the true normalised mass gain of each sample.

Oxidised samples were embedded in conductive DemoTec 70 polymer before being polished to reveal the cross section and imaged with an SEM. Samples were not etched to preserve the chemical composition of the oxides. Cross sections were characterised with energy-dispersive X-ray analysis (EDX) via line scans and distribution maps. The oxidised samples were removed from the polymer mechanically and with acetone. X-ray diffraction patterns of the near-surface zone of the samples were recorded using the X-ray diffractometer ETA (GE XRD 3003) equipped with a long fine Co-X-ray tube and a DECTRIS MYTHEN2R

1D detector. Measurements were performed in the angle-dispersive (AD) mode of diffraction. To obtain phase information from larger depths, the LIMAX-160 diffractometer equipped with a liquid metal jet X-ray source (MetalJet D2 160 kV) and a Low Energy Germanium (LEGe) detector operated in the energy-dispersive (ED) mode of diffraction was used. In the AD mode of diffraction, data points are recorded through  $\theta$ - $\theta$  X-ray tube/detector scans (Bragg-Brentano geometry), while in the ED mode of diffraction, complete diffraction patterns with a multitude of diffraction lines are measured for a fixed position of the sample and the detector.

## Results and discussion

### Short-term oxidation experiments

Ni–Fe–Cu alloys in the as-cast condition have been shown to perform worse during dry oxidation and aluminium electrolysis by Gallino et al. [10] due to the presence of two FCC Ni–Fe-rich (dendrites) and Cu-rich (matrix) phases which cause a galvanic coupling effect, accelerating corrosion. Figure 1 shows the typical microstructure of as-cast vs homogenised samples of Ni<sub>42</sub>Fe<sub>38</sub>Cu<sub>20</sub> wt.%, representative of this ternary system. The single-phase structure is clearly displayed in Fig. 1b, confirming previous studies of a reduced miscibility gap in this region by Gallino et al. [8], where homogenisation was achieved for each alloy using the same protocol of heating to 1100 °C and annealing for 12 h. Measuring the oxidation behaviour of each alloy at 800 °C for 18 h under 1 atm of O<sub>2</sub> flux allowed for the parabolic rate constant  $k_p$  to be calculated in Fig. 2 for each temperature using the parabolic rate equation of  $(\Delta M)^2 = k_p \Delta t$  where  $\Delta M$  is the normalised (by surface area cm<sup>2</sup>) mass gain and  $t$  is the oxidation time.

Oxidation behaviour of homogenised Ni<sub>60</sub>Fe<sub>30</sub>Cu<sub>10</sub> wt.%, Ni<sub>42</sub>Fe<sub>38</sub>Cu<sub>20</sub> wt.% and Ni<sub>29</sub>Fe<sub>59</sub>Cu<sub>15</sub> wt.% can be seen in Fig. 3. Fitting the data in accordance with the power law  $(\Delta M)^m = k_m \Delta t + C$  allows the different behavioural regimes to become clearly distinguished. It is common during the oxidation of alloys to have many competing mechanisms superimposed over one another and for  $m$  to be a non-integer value upon fitting the data. Figure 2b confirms the close adherence to a pure parabolic rate law ( $m = 2$ ). The  $m$  values and the corresponding parabolic rate constant

**Figure 1** Optical microscope images (a) and (b) show the as-cast and homogeneous microstructure of  $\text{Ni}_{42}\text{Fe}_{38}\text{Cu}_{20}$  wt.%, respectively, representative of each alloy in this study. Single-phase microstructure was achieved via annealing at 1100 °C for 12 h.

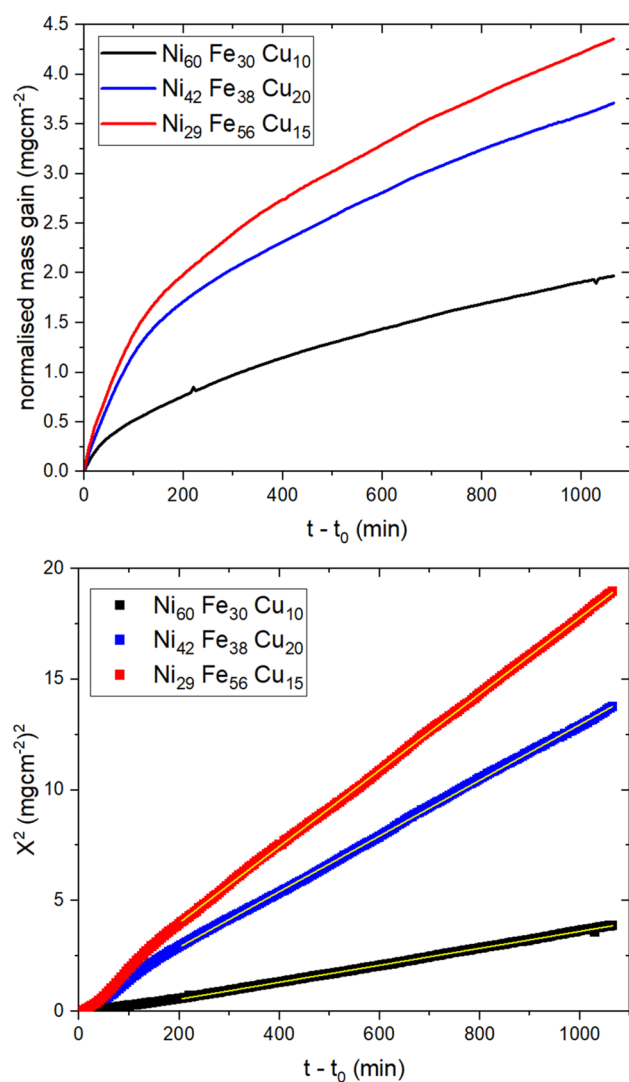
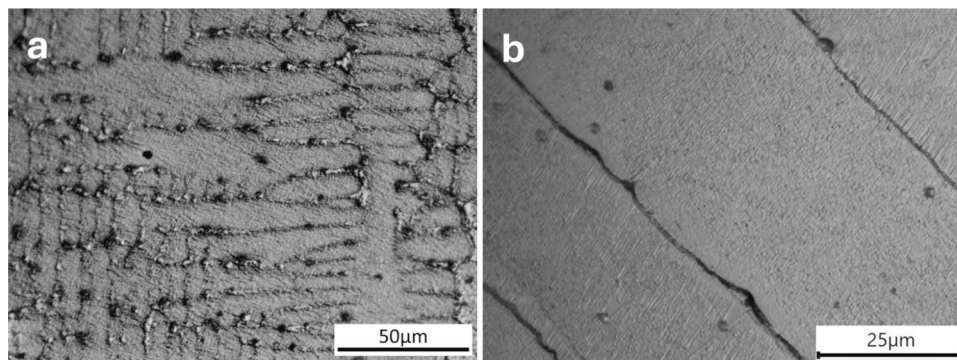


**Figure 2** TGA weight gain variation studies with oxidation time. Oxidation evolution of homogeneous  $\text{Ni}_{60}\text{Fe}_{30}\text{Cu}_{10}$  wt.%,  $\text{Ni}_{42}\text{Fe}_{38}\text{Cu}_{20}$  wt.% and  $\text{Ni}_{29}\text{Fe}_{56}\text{Cu}_{15}$  wt.% under 1 atm of  $\text{O}_2$  at 800 °C for 18 h where  $X$  is the normalised mass gain. Each alloy was confirmed to follow a parabolic rate behaviour.

**Table 1** Oxidation data of homogenised  $\text{Ni}_{60}\text{Fe}_{30}\text{Cu}_{10}$  wt.%,  $\text{Ni}_{42}\text{Fe}_{38}\text{Cu}_{20}$  wt.%, and  $\text{Ni}_{29}\text{Fe}_{56}\text{Cu}_{15}$  wt.% under 1 atm  $\text{O}_2$  at 800 °C for 18 h

Composition	Avg. scale thickness (μm)	Mass gain $m$ (mg cm <sup>-2</sup> )	$k_p$ (mg <sup>2</sup> cm <sup>-4</sup> s <sup>-1</sup> )
$\text{Ni}_{60}\text{Fe}_{30}\text{Cu}_{10}$	24.22	2.44	$1.80 \times 10^{-5}$
$\text{Ni}_{42}\text{Fe}_{38}\text{Cu}_{20}$	39.73	4.38	$2.15 \times 10^{-5}$
$\text{Ni}_{29}\text{Fe}_{56}\text{Cu}_{15}$	42.73	5.25	$5.86 \times 10^{-4}$

data are displayed in Table 1. The variable oxidation rate between the three alloys can be broadly correlated to their respective Fe content, where the least Fe-rich alloy  $\text{Ni}_{60}\text{Fe}_{30}\text{Cu}_{10}$  wt.% has the slowest rate of oxidation. Previous studies on Ni–Fe–Cu oxidation lean towards a higher copper and iron content, with complex kinetic behaviour at low temperatures (750–850 °C), following parabolic rate behaviour in the best case scenario [3, 7, 10, 15–19], in agreement with the data presented in Table 1. The parabolic rate constants of the oxidation of pure iron ( $5 \times 10^{-7} \text{ g}^2\text{cm}^4\text{s}^{-1}$ ), copper ( $8 \times 10^{-8} \text{ g}^2\text{cm}^4\text{s}^{-1}$ ) and nickel ( $4 \times 10^{-10} \text{ g}^2\text{cm}^4\text{s}^{-1}$ ) [17] with the help of an Ellingham diagram [17, 20] make it apparent how a greater percentage of iron significantly increases the oxidation rate. The parabolic rate constants of  $\text{Ni}_{60}\text{Fe}_{30}\text{Cu}_{10}$  wt.% and  $\text{Ni}_{42}\text{Fe}_{38}\text{Cu}_{20}$  wt.% obtained for this alloy are of the same order of magnitude as Jucken et al. where  $\text{Cu}_{65}\text{Ni}_{20}\text{Fe}_{15}$  wt.% was used [16]. The alloys in this study were however oxidised at 800 °C in pure oxygen, whereas Jucken et al. oxidised  $\text{Cu}_{65}\text{Ni}_{20}\text{Fe}_{15}$  wt.% in air (lower oxygen pressure), at only 700 °C. From this it can be concluded that higher oxidation resistance in Ni–Fe-rich alloys compared to Cu-rich alloys in this ternary system is expected. In Table 1 the parabolic rate constant of  $\text{Ni}_{29}\text{Fe}_{56}\text{Cu}_{15}$  wt.% shows an order of magnitude increase

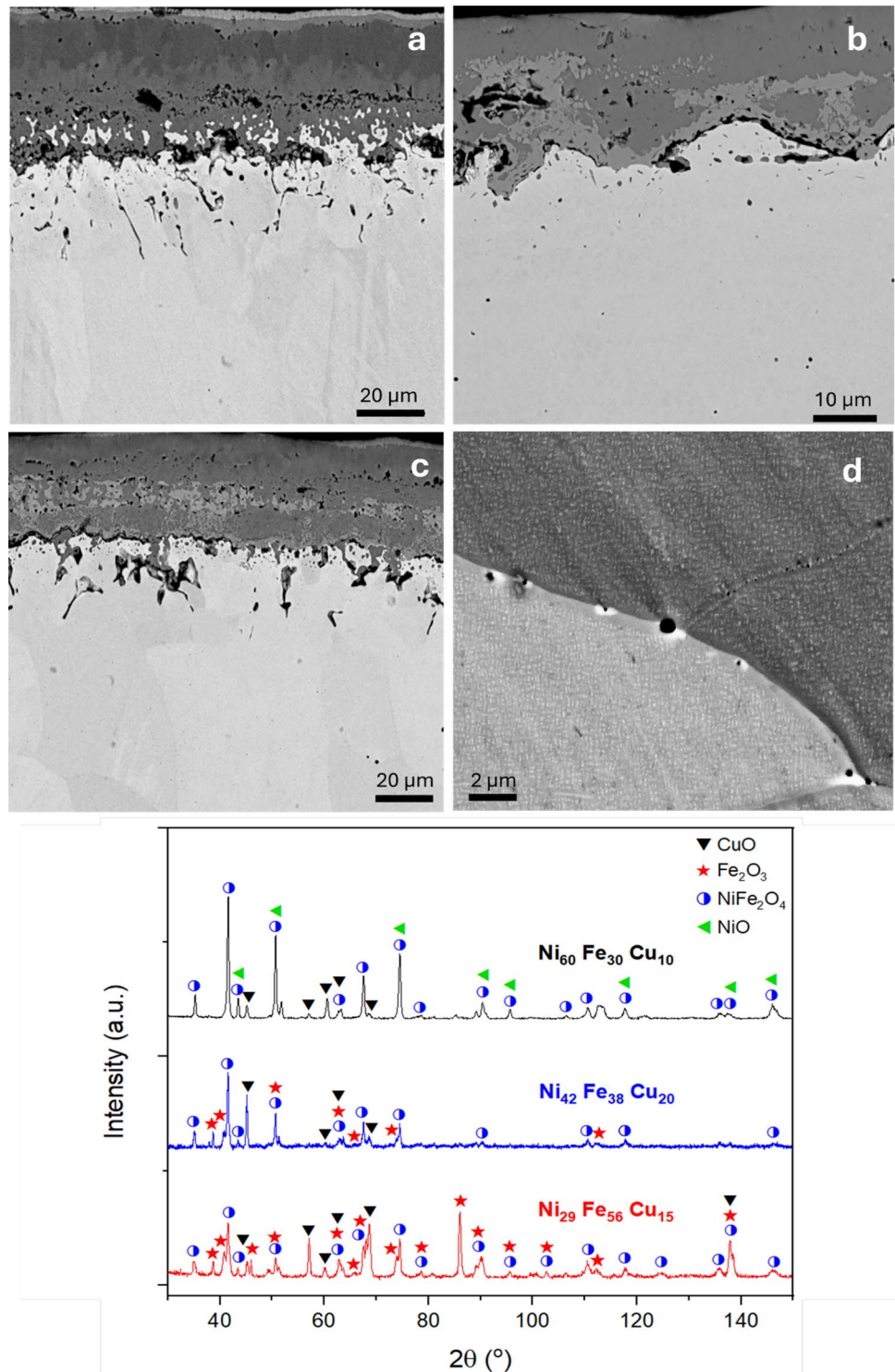


compared to the other alloys, highlighting the sensitivity of this system to the specific Fe content.

Figure 3 shows the primary oxides present in each alloy after 18 h of oxidation. CuO oxide formation on the surface was consistent across all three

alloys, as well as an internal  $\text{NiFe}_2\text{O}_4$  layer at the alloy–oxide interface. The  $\text{NiFe}_2\text{O}_4$  region appeared largest for the  $\text{Ni}_{42}\text{Fe}_{38}\text{Cu}_{20}$  wt.% alloy, which was observed to include small amounts of  $\text{Fe}_2\text{O}_3$  and NiO dispersed throughout the scale in Fig. 3c. NiO

**Figure 3** Microstructural and structural analysis of samples after oxidation. **a**, **b** and **c** show BSE cross sections of  $\text{Ni}_{29}\text{Fe}_{59}\text{Cu}_{15}$  wt.%,  $\text{Ni}_{60}\text{Fe}_{30}\text{Cu}_{10}$  wt.% and  $\text{Ni}_{42}\text{Fe}_{38}\text{Cu}_{20}$  wt.%, respectively, each after 18 h of oxidation under 1 atm of  $\text{O}_2$  at 800 °C. Spinodal decomposition of the Ni–Fe–Cu  $\gamma$ -FCC phase into NiFe  $\gamma$ -FCC and Cu  $\gamma$ -FCC-rich phases is shown for  $\text{Ni}_{29}\text{Fe}_{59}\text{Cu}_{15}$  wt.% in **(d)** due to the critical Fe and Cu content. XRD spectra of each alloy are shown in **(e)** where the assignment of NiO and  $\text{NiFe}_2\text{O}_4$  was assisted by BSE/EDX data due to the overlapping reflections of these phases.



could not be clearly identified in the XRD spectrum of  $\text{Ni}_{42}\text{Fe}_{38}\text{Cu}_{20}$  wt.% despite being observed in BSE/EDX images—likely due to the small and incoherent patterns it forms in the scale.  $\text{Ni}_{29}\text{Fe}_{56}\text{Cu}_{15}$  wt.% oxidises to form a dominant  $\text{Fe}_2\text{O}_3$  layer (dark grey oxide region in Fig. 3a) with no visible NiO. The  $\text{Ni}_{60}\text{Fe}_{30}\text{Cu}_{10}$  wt.% alloy is primarily characterised by a large internal NiO layer directly at the alloy–oxide interface.

The outward diffusion of copper causes an initial CuO layer to form. Subsequent oxidation is then dominated by iron, with copper and nickel partitioning out of the scale. EDX images show a visible copper and nickel enrichment in the bulk below the scale in all cases. An internal oxidation of nickel-rich material occurs forming NiO, which, in the presence of enough  $\text{Fe}_2\text{O}_3$ , leads to  $\text{NiFe}_2\text{O}_4$  formation. A lack of copper oxides at the alloy–oxide interface suggests the continuous diffusion of copper through the scale.

$\text{Ni}_{29}\text{Fe}_{56}\text{Cu}_{15}$  wt.% displayed coarse spinodal decomposition within the bulk due to a low nickel content and critical iron and copper content, while the single-phase structure of  $\text{Ni}_{42}\text{Fe}_{38}\text{Cu}_{20}$  wt.% and  $\text{Ni}_{60}\text{Fe}_{30}\text{Cu}_{10}$  wt.% appeared to remain intact.

### Long-term oxidation behaviour of $\text{Ni}_{42}\text{Fe}_{38}\text{Cu}_{20}$ wt.% and $\text{Ni}_{60}\text{Fe}_{30}\text{Cu}_{10}$ wt.%

Long-term oxidation behaviour of homogenised  $\text{Ni}_{42}\text{Fe}_{38}\text{Cu}_{20}$  wt.% and  $\text{Ni}_{60}\text{Fe}_{30}\text{Cu}_{10}$  wt.% can be seen in Fig. 4 which shows the mass gain per  $\text{cm}^2$  of each alloy over 272 h of the isothermal run, baseline subtracted. Taking the double-log plot of each signal allows  $m$  to be calculated and the rate behaviour to be defined. Fitting the TGA data for  $\text{Ni}_{42}\text{Fe}_{38}\text{Cu}_{20}$  wt.% gives  $m = 2.83$  after 30 h of oxidation as shown in Fig. 4b, which can be said to approximate to cubic behaviour where a purely cubic oxidation law would give  $m = 3$ . The alloy follows parabolic behaviour for approximately the first 21 h (stage I), a transition period of accelerated linear-like behaviour follows (stage II) (also observed separately in the 72-h oxidation, not pictured), and thereafter, a stable cubic behaviour is observed from 30 to 300 h (stage III). Points  $t = 112$  h and  $t = 242$  h during stage III show accelerated oxidation rate for approximately 7 h and 5 h, respectively, after which typical behaviour is resumed, potentially indicative of oxide spalling and subsequent healing.

$\text{Ni}_{60}\text{Fe}_{30}\text{Cu}_{10}$  wt.% follows a similar pattern of transition from a parabolic to a cubic rate behaviour. In this case, cubic rate behaviour does not emerge until

approximately 264 h ( $m = 2.86$ ) of isothermal oxidation as shown in Fig. 4c. Moments of accelerated oxidation due to potential spalling are not visible. The more rapid initial oxidation of  $\text{Ni}_{42}\text{Fe}_{38}\text{Cu}_{20}$  wt.% leads to a thicker scale which appears to have a greater passivating effect on continued internal oxidation as internal oxygen diffusion is inhibited, thus reaching a cubic regime much more quickly than the slower growing  $\text{Ni}_{60}\text{Fe}_{30}\text{Cu}_{10}$  wt.%. Both alloys appear to transition to a cubic behaviour at approximately similar mass gain values ( $\sim 5 \text{ mg cm}^{-2}$ ) which suggests a quasi-threshold effect, beyond which oxidation is sufficiently passivated as to transition to a cubic regime. The NiO-driven mechanism of  $\text{Ni}_{60}\text{Fe}_{30}\text{Cu}_{10}$  wt.% takes much longer to reach this threshold—as opposed to  $\text{Ni}_{42}\text{Fe}_{38}\text{Cu}_{20}$  wt.% where a greater Fe content drives a higher oxidation rate.

Figure 5 shows the typical oxide morphology of  $\text{Ni}_{42}\text{Fe}_{38}\text{Cu}_{20}$  wt.% after 300 h of oxidation and for  $\text{Ni}_{60}\text{Fe}_{30}\text{Cu}_{10}$  wt.% after 272 h of oxidation. A greater divergence in scale composition is visible, in comparison with Fig. 3,  $\text{Ni}_{60}\text{Fe}_{30}\text{Cu}_{10}$  wt.% is dominated by NiO formation throughout the scale in somewhat non-uniform patterns. Columns of Fe-rich oxide, likely  $\text{NiFe}_2\text{O}_4$ , interrupt NiO formations. These iron-enriched regions and subsequent Fe-rich columns may come from iron diffusion into the more oxygen-rich grain boundaries. The oxide morphology that forms in  $\text{Ni}_{60}\text{Fe}_{30}\text{Cu}_{10}$  wt.% was indeed largely observed to be much less uniform than in  $\text{Ni}_{42}\text{Fe}_{38}\text{Cu}_{20}$  wt.%. Figure 5 shows that the  $\text{Ni}_{42}\text{Fe}_{38}\text{Cu}_{20}$  wt.% alloy favours a more compact, uniform (Ni, Fe)O spinel region, with some small amount of incoherent NiO patterns at the alloy–oxide interface. Continued penetration of the oxygen beneath the scale was observed to be more prominent in  $\text{Ni}_{60}\text{Fe}_{30}\text{Cu}_{10}$  wt.%, potentially due to favourable iron oxidation along the grain boundaries. Early oxidation favours Fe-oxide formation, beneath which lays a Cu and especially Ni-enriched region. This heavily Ni-enriched substrate oxidises preferentially to form NiO. NiO formation possesses a higher driving force of oxidation than  $\text{Fe}_2\text{O}_3$  evolution from  $\text{Fe}_3\text{O}_4$ , inhibiting (Ni, Fe)O spinel formation in these regions [6, 7, 17]. The efficacy of the NiO structures as a diffusion barrier against oxygen causes preferential oxygen diffusion around them, through Fe-oxide regions and along grain boundaries. This effect becomes more exaggerated over time as the NiO layer thickens and likely contributes to the non-uniformity of

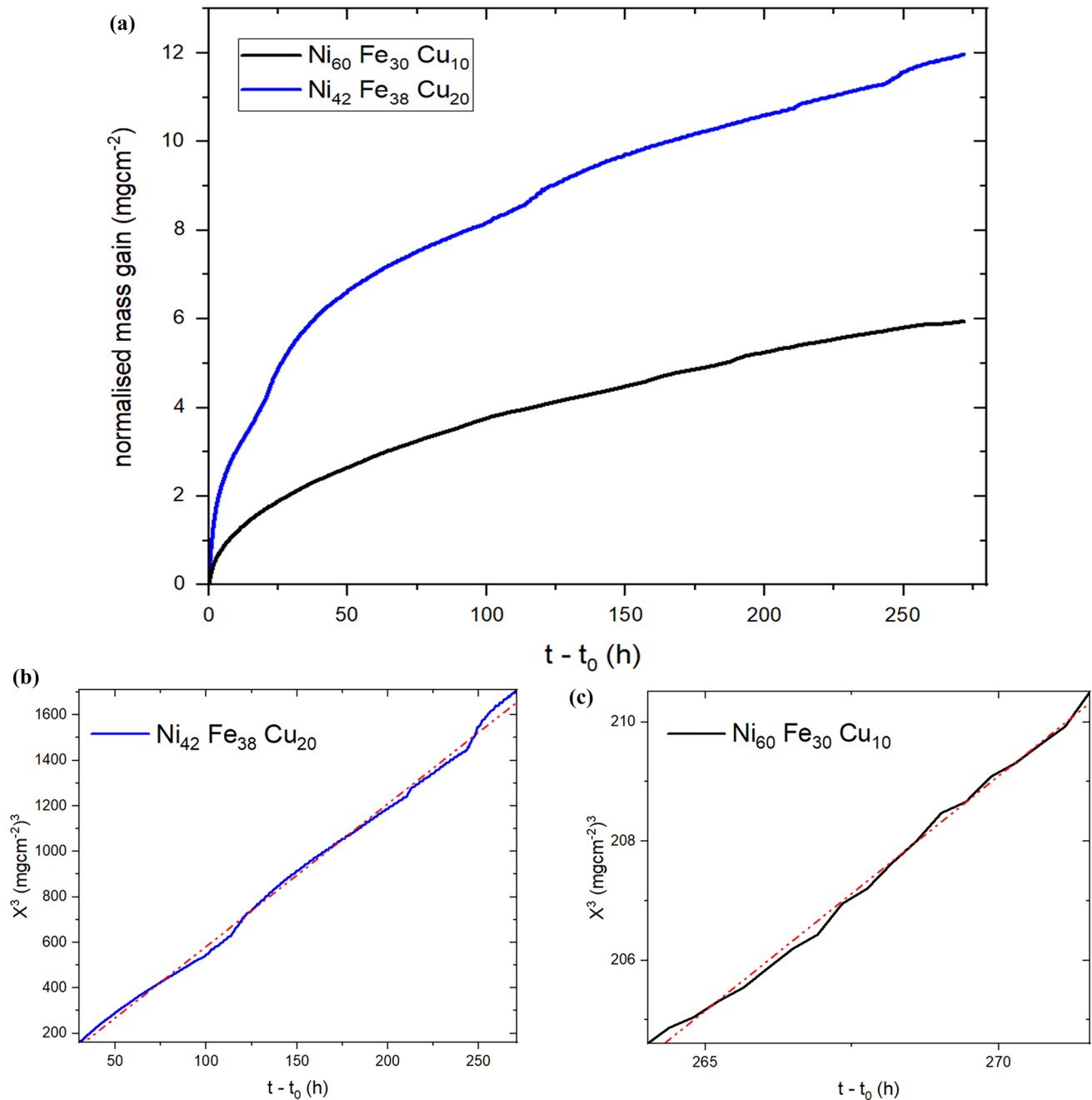


**Figure 4** TGA mass gain over 272 h of oxidation under 1 atm of  $\text{O}_2$  at 800 °C (a) for  $\text{Ni}_{42}\text{Fe}_{38}\text{Cu}_{20}$  wt.% and  $\text{Ni}_{60}\text{Fe}_{30}\text{Cu}_{10}$  wt.%. Adherence to a cubic rate behaviour is shown in (b) from  $t \geq 30$  h for  $\text{Ni}_{42}\text{Fe}_{38}\text{Cu}_{20}$  wt.%, and in (c) from  $t \geq 264$  h for  $\text{Ni}_{60}\text{Fe}_{30}\text{Cu}_{10}$  wt.%.

the  $\text{Ni}_{60}\text{Fe}_{30}\text{Cu}_{10}$  wt.% scale observed in Fig. 5. Fe-oxidation then occurs predominantly in these more oxygen-rich regions between NiO structures, aided as well by the greater diffusivity of Fe cations than Ni cations [17], where  $\text{Fe}_2\text{O}_3$  can seemingly form and then react with nearby NiO to form  $\text{NiFe}_2\text{O}_4$ . The end result for  $\text{Ni}_{60}\text{Fe}_{30}\text{Cu}_{10}$  wt.% is relatively thick

columnar formations of NiO occasionally punctuated by thinner (Ni, Fe)O regions.

Figure 6 shows a local region of the  $\text{Ni}_{60}\text{Fe}_{30}\text{Cu}_{10}$  wt.% alloy at which more extensive oxidation occurred. The scale can be seen to have partially blistered, allowing a penetration depth of  $\geq 0.5$  mm of the oxygen and extensive intergranular corrosion.



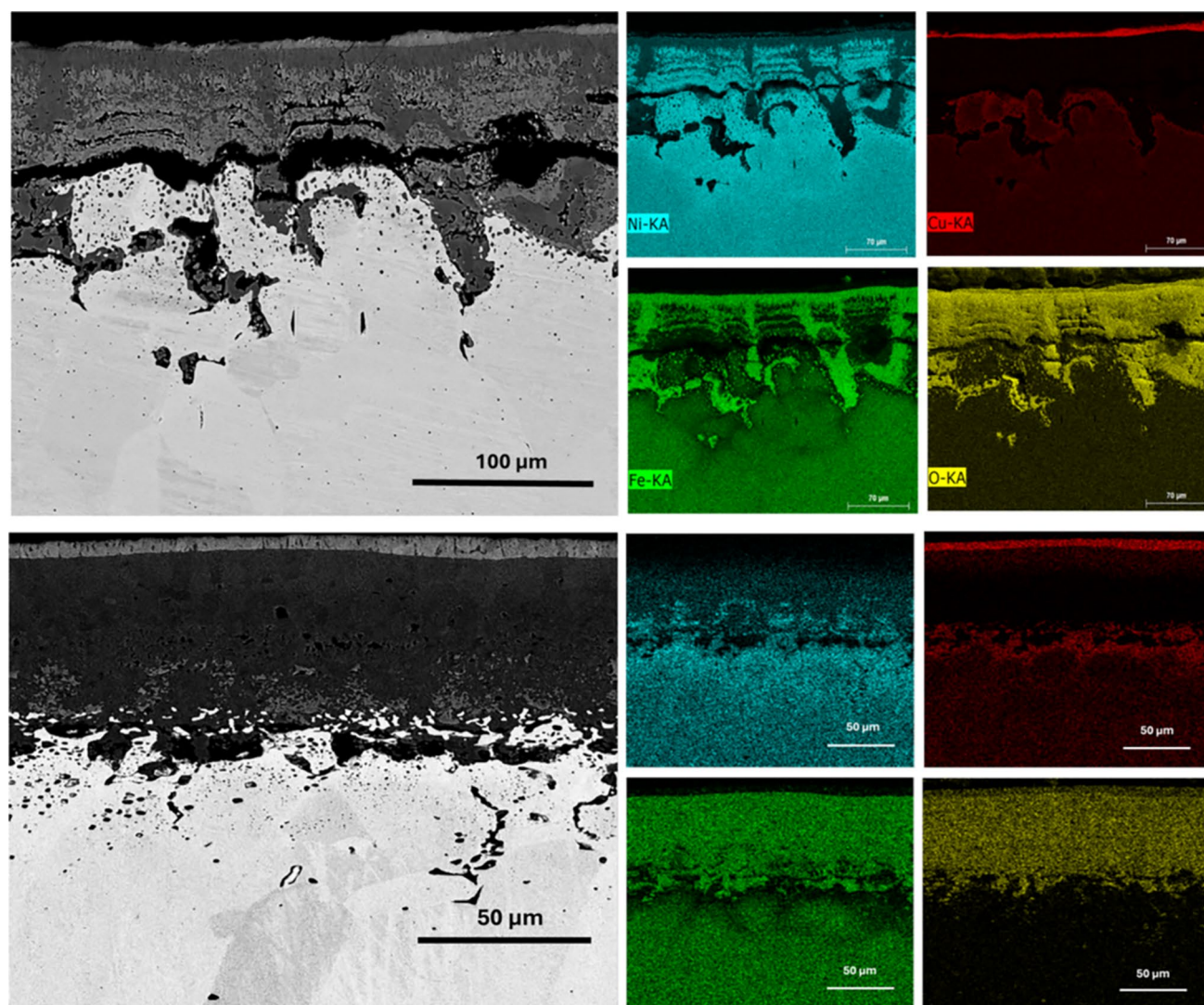


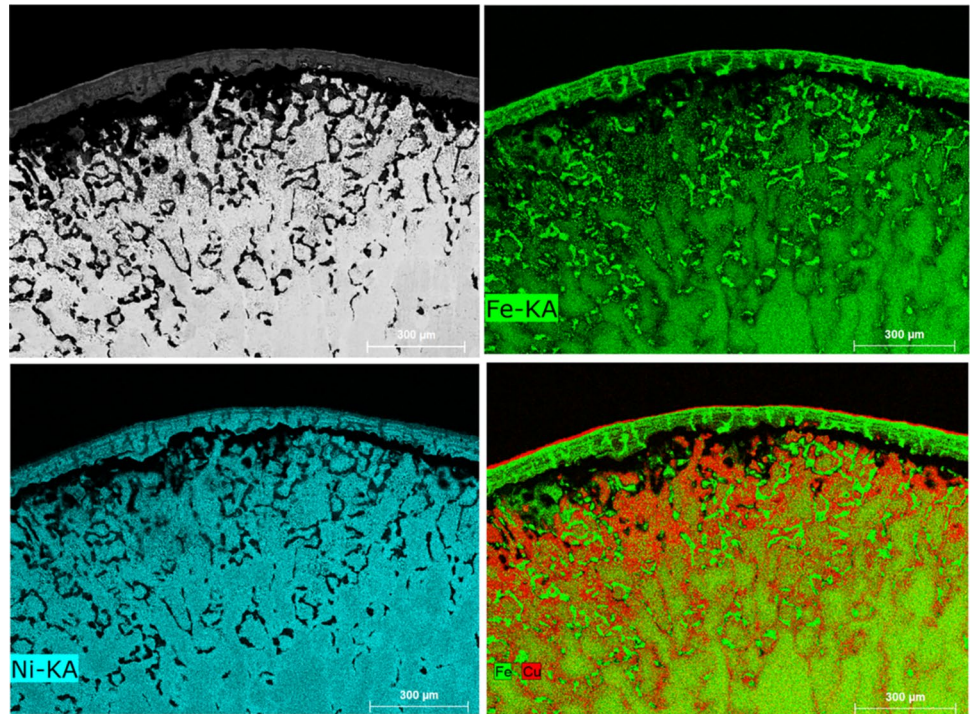
**Figure 5** BSE and EDX cross sections of homogenous  $\text{Ni}_{60}\text{Fe}_{30}\text{Cu}_{20}$  wt.% (top) and  $\text{Ni}_{42}\text{Fe}_{38}\text{Cu}_{20}$  wt.% (bottom) oxidised at 800 °C under 1 atm of  $\text{O}_2(\text{g})$  for 300 h and 272 h, respectively.

Iron depletion and subsequent copper and nickel enrichment are observed along the grain boundaries. Initially, the iron preferentially segregates along grain boundaries in the presence of oxygen, and then oxidises between grains, leaving behind a relative Ni and Cu enrichment. In  $\text{Ni}_{60}\text{Fe}_{30}\text{Cu}_{10}$  wt.%, the lowered but not insignificant Fe content appears to drive the alloy towards substantial grain boundary oxidation iron, leading to a less compact scale formation and the possibility of embrittlement and cracking [21–23]. While the iron oxides in the scale are able to—in the presence of NiO—form (Ni, Fe)O oxides, the intergranular oxidation beneath the scale appears to lead to less favourable (with respect to

cryolite solubility) Fe oxides. Additionally, the poor adherence of the scale as observed in Fig. 6 would likely lend itself to ample penetration and attack from the electrolyte. The formation instead of a large, uniform and well adhered (Ni, Fe)O region favours strong electrolysis performance, due to the relative insolubility of  $\text{NiFe}_2\text{O}_4$  in cryolite-based solutions [3–5], as is the case for  $\text{Ni}_{42}\text{Fe}_{38}\text{Cu}_{20}$  wt.%. The irregular oxide morphology observed in  $\text{Ni}_{60}\text{Fe}_{30}\text{Cu}_{10}$  wt.% could also result in differing dissolution rates across parts of the scale during electrolysis, as opposed to a more steady and uniform dissolution. A direct comparison of the long-term electrolysis performance of differing Ni:Fe ratios and their influence on oxide



**Figure 6** BSE and EDX mapping of homogeneous  $\text{Ni}_{60}\text{Fe}_{30}\text{Cu}_{10}$  wt.% after oxidation at 800 °C for 272 h under 1 atm of  $\text{O}_2(\text{g})$ . Extensive local inter-granular oxidation is observed with Fe oxides forming predominantly in the depletion zone between grains beneath the scale, indicated by green spots of greater intensity.



products in Ni–Fe–Cu anodes would be beneficial, in a future study.

### Oxidation mechanism of $\text{Ni}_{42}\text{Fe}_{38}\text{Cu}_{20}$ wt. %

Long-term oxidation behaviour of the homogenised  $\text{Ni}_{42}\text{Fe}_{38}\text{Cu}_{20}$  wt.% can be seen in Fig. 7, along with the double-log plot, which shows the mass gain per  $\text{cm}^2$  of the alloy over the entire 300 h of the isothermal run, baseline subtracted. Individual oxidation runs of five separate isothermal times, allowing subsequent EDX/XRD analysis of the cross sections, are labelled in Fig. 7. Stability of the cubic rate behaviour remained stable from 272 to 300 h of the longest isothermal run, as previously documented in Fig. 4.

Figure 8 shows the diffraction patterns of the 5-h (shortest) and 300-h (longest)  $\text{Ni}_{42}\text{Fe}_{38}\text{Cu}_{20}$  wt.% oxidation samples. Oxide scale thickness and TGA data for all oxidation samples in this range is displayed in (Table 2). The presence of  $\text{NiFe}_2\text{O}_4$  is confirmed already at the shortest oxidation time of 5 h.  $\text{CuO}$ ,  $\text{Fe}_2\text{O}_3$  and  $\text{NiFe}_2\text{O}_4$  phases can be clearly matched to reference patterns in the 5-h sample, up to the 18-h sample (not shown). Figure 8 shows how the  $\text{CuO}$  peak intensity increases with time—meaning copper is still able to diffuse through the thicker scale and oxidise further. For the 72-h (not shown) and 300-h samples, a marked difference is observed. The continued internal growth

of nickel ferrite that one expects does not translate to greater peak intensity for the associated reference peaks. Rather, the noticeable appearance of a  $\text{CuFe}_2\text{O}_4$  phase underneath the external  $\text{CuO}$  layer now exists and the deeper-laying  $\text{NiFe}_2\text{O}_4$  layer is masked by the  $\text{CuFe}_2\text{O}_4$  phase. This results in the  $\text{CuO}$ ,  $\text{Fe}_2\text{O}_3$  and  $\text{CuFe}_2\text{O}_4$  patterns becoming the most clear for the 72-h and 300-h samples. The preferential representation of the  $\text{CuFe}_2\text{O}_4$  phase over time is more clearly displayed in Fig. 8. In the 72-h and 300-h spectra (72 h not shown) gradual suppression of the  $\text{Fe}_2\text{O}_3$  peaks can be observed likely due to the consumption of this phase as it forms copper and nickel ferrite via  $\text{CuO} + \text{Fe}_2\text{O}_3 \rightarrow \text{CuFe}_2\text{O}_4$  and  $\text{NiO} + \text{Fe}_2\text{O}_3 \rightarrow \text{NiFe}_2\text{O}_4$  reactions. In Fig. 10 immediately below the  $\text{CuO}$  layer, a gradual inverse relationship between the Cu wt.% and Ni wt.% is observed as  $\text{CuFe}_2\text{O}_4$  dominance shifts to  $\text{NiFe}_2\text{O}_4$  dominance deeper into the scale—with the implication of a mixed  $(\text{Ni,Cu})\text{Fe}_2\text{O}_4$  spinel in a solid solution due to the continuous change in Cu and Ni concentrations, that eventually gives way to a dominant  $\text{NiFe}_2\text{O}_4$  region at a depth of approximately 45  $\mu\text{m}$ . Such intermediate  $\text{Cu}_{(1-x)}\text{Ni}_x\text{Fe}_2\text{O}_4$  phases have been documented before [24–26], with XRD spectra that did not necessarily match to Fig. 8. The peaks at  $2\theta = 40.8^\circ$ ,  $2\theta = 41.9^\circ$ ,  $2\theta = 49.2^\circ$  and  $2\theta = 66.0^\circ$  become distinguishable at  $t = 300$  h and likely correspond to a  $\text{CuFe}_2\text{O}_4$  phase. Figures 8 and 10 seem to suggest the presence

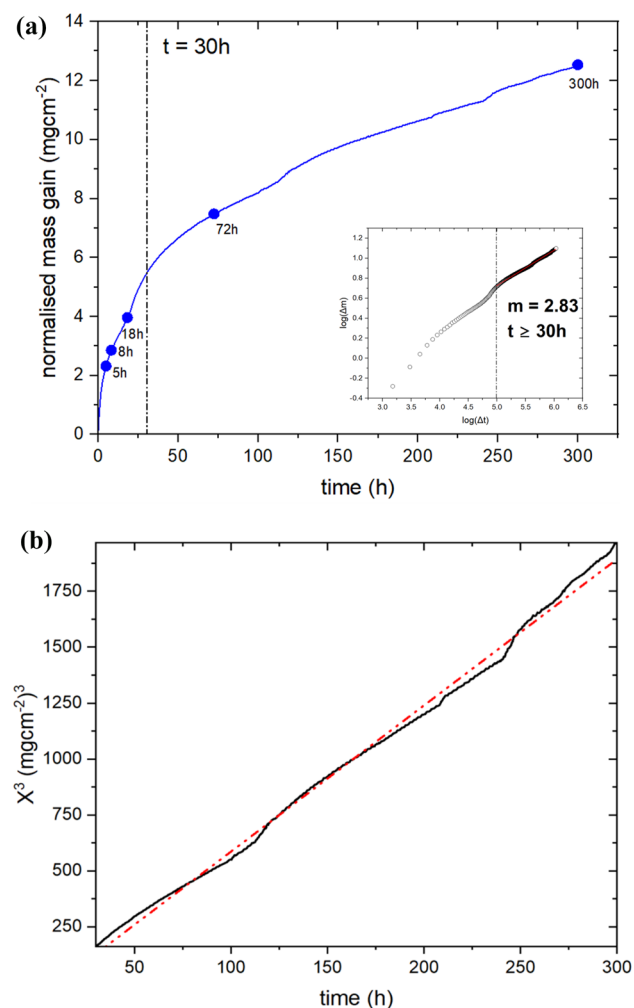


**Figure 7** TGA of the oxidation evolution of homogeneous  $\text{Ni}_{42}\text{Fe}_{38}\text{Cu}_{20}$  wt.% in 1 atm of  $\text{O}_2(\text{g})$  at  $800^\circ\text{C}$  where the points in (a) each represent separate oxidation studies and their respective isothermal run times.  $t = 30$  h represents a shift from parabolic to approximately cubic rate behaviour. The x-axis of the double-log plot (inset) in (a) was calculated with seconds,  $\log(\text{s})$ . Taking a linear fit (b)—the strong adherence ( $R^2 = 0.996$ ) to a cubic behaviour from 30 to 300 h is shown where  $X$  is the normalised mass gain.

**Table 2** Average scale thickness and rate behaviour of homogenised  $\text{Ni}_{42}\text{Fe}_{38}\text{Cu}_{20}$  wt.% under 1 atm of  $\text{O}_2$  at  $800^\circ\text{C}$  for each measurement. Normalised mass gain displayed from Fig. 1 for corresponding times

Time h	Avg. scale thickness $\mu\text{m}$	Mass gain per $\text{cm}^2$ $\text{mg cm}^{-2}$	Parabolic constant $k_p$ $\text{mg}^2 \text{cm}^{-4} \text{s}^{-1}$	Cubic constant $k_c$ $\text{mg}^3 \text{cm}^{-6} \text{s}^{-1}$
5	18.54	2.77		—
8	32.80	3.28	$2.82 \times 10^{-5}$	—
18	39.73	4.38		—
72	54.93	7.93	—	$1.16 \times 10^{-3}$
300	104.28	12.98	—	

of both distinct  $(\text{Cu/Ni})\text{Fe}$ , O spinel phases and the possibility of a mixed  $(\text{Cu,Ni})\text{Fe}_2\text{O}_4$ , respectively. Future investigations into the interactions between copper and nickel spinel structures during oxidation are necessary to gain a better understanding.

Figure 9 displays the measured spectra of the oxides for the 72-h and 300-h oxidised samples. In this energy-dispersive mode, a deeper penetration of the scale is possible and the internal Fe-rich phases are able to be illuminated—including the  $\text{NiFe}_2\text{O}_4$  phase particularly at longer oxidation times where the scale is thickest. The  $\text{Fe}_3\text{O}_4$  phase is also particularly difficult to separate from the  $\text{NiFe}_2\text{O}_4$  phase due to both possessing similar lattice parameters. The presence of NiO could not be confidently confirmed in the XRD experiments. Back-scattered electron (BSE) imaging and EDX mapping such as in Figs. 5 and 11, reveal a clear nickel enrichment in the oxide scale. The small quantities of NiO in the scale as well as its position close to the alloy–oxide interface explain its lack of representation in Fig. 5. The line scan from Fig. 10 also shows evidence of a deep-laying  $\text{Fe}_3\text{O}_4$  region, which is in agreement with findings from Jucken et al. [16], hence the inclusion in Fig. 9. The phases assigned in Fig. 9 could also be assigned to the oxidation scales of the 5-h, 8-h and 18-h samples which are not shown here. The angle-dispersive diffraction mode, which may struggle to illuminate internal oxides, is sufficient in showing the relatively slow growth of the  $\text{CuFe}_2\text{O}_4$  phase that becomes much more noticeable in the diffraction pattern after 18 h of oxidation, from Fig. 8.  $\text{NiFe}_2\text{O}_4$  formation is clearly distinguished from 5 to 18 h. At longer oxidation times energy-dispersive diffraction is able to more easily illuminate this phase.

Figure 10 reveals how the oxide phases prefer to layer themselves within the scale. The line scan analysis reveals the  $(\text{Ni, Fe})\text{O}$  spinel region possesses a Ni:Fe atomic weight ratio of approximately 1:2 which one would expect of  $\text{NiFe}_2\text{O}_4$  and is therefore a strong

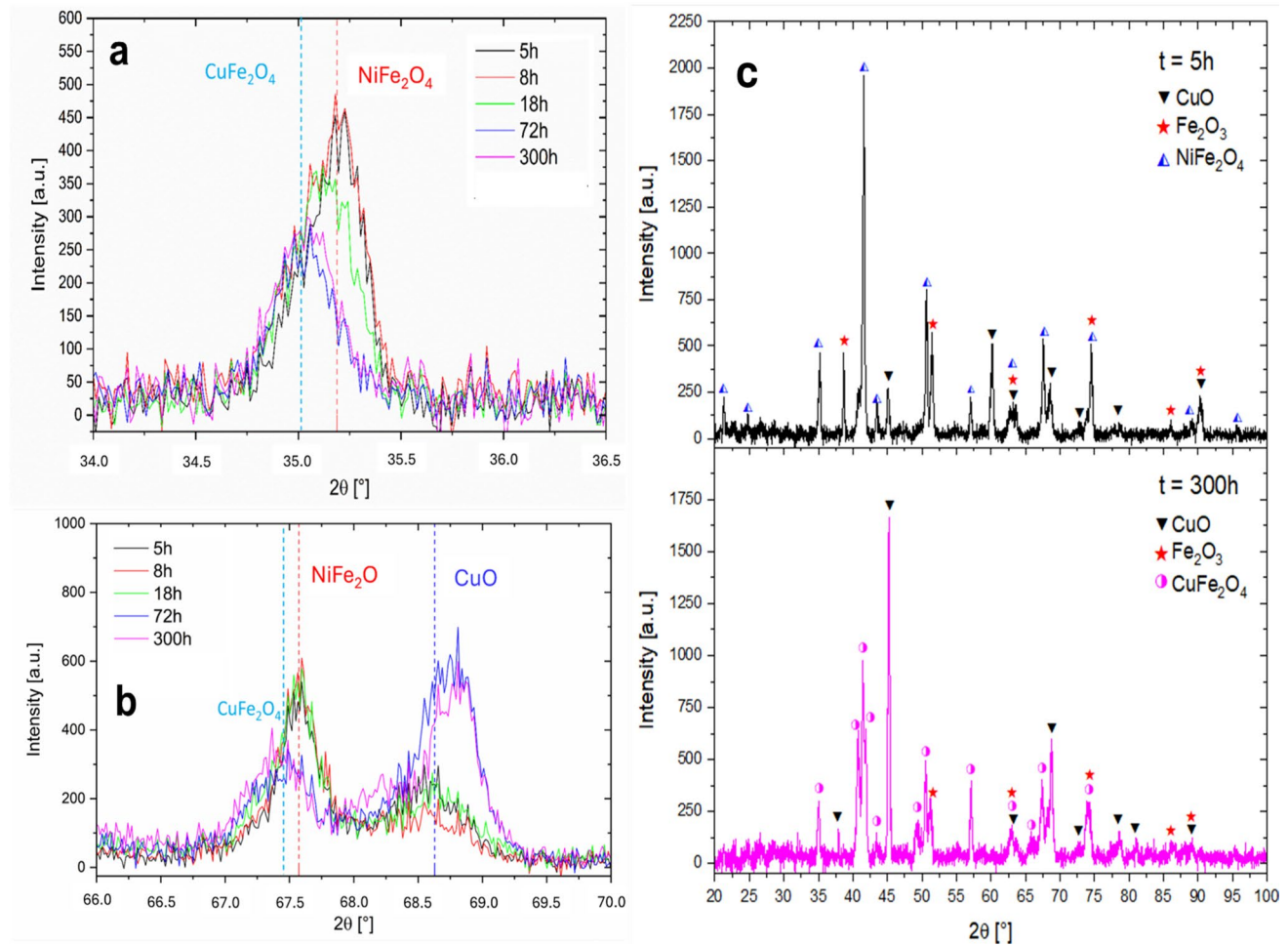


**Figure 8** XRD study of the oxide scales. **a** and **b** show overlapping angle-dispersive XRD spectra from all oxidised  $\text{Ni}_{42}\text{Fe}_{38}\text{Cu}_{20}$  wt.% homogeneous samples. A subtle shift towards the  $\text{CuFe}_2\text{O}_4$  reflection at longer oxidation times becomes visible. Similar lattice parameters between both the  $\text{NiFe}_2\text{O}_4$  and  $\text{CuFe}_2\text{O}_4$  phase can make the reflections hard to distinguish.

indicator of a thick, uniform nickel ferrite layer. The scale exhibits a non-repeating pattern, with continued growth at 300 h being predominantly driven by an internal growth of the  $\text{NiFe}_2\text{O}_4$  phase which appears to consist of approximately 70% of total scale thickness according to Fig. 10 and a second EDX line scan that is not shown. The profile of oxides across the observed cross section showed good uniformity.

Three key points appear to prevent a repeating oxide layer structure from forming:

- Copper diffusion to the surface from the alloy is not prevented, as the external  $\text{CuO}$  and  $\text{CuFe}_2\text{O}_4$  layers are both observed to grow over time.

The growth of the  $\text{NiFe}_2\text{O}_4$  phase deeper into the alloy over time becomes less visible as the X-ray intensity is absorbed by the growing  $\text{CuFe}_2\text{O}_4$  phase. The continued growth of the  $\text{CuO}$  phase is also displayed. For contrast, **c** shows a wider XRD spectra of homogenised  $\text{Ni}_{42}\text{Fe}_{38}\text{Cu}_{20}$  wt.% oxidised for 5 h and 300 h at 800 °C.

- Local nickel enrichment at the alloy–oxide interface leads to  $\text{NiO}$  clusters forming in this region.  $\text{NiO}$  clusters seed the continued reaction with  $\text{Fe}_2\text{O}_3$  to form  $\text{NiFe}_2\text{O}_4$  internally.
- Finally, the scale up to 300 h remains well adhered to the alloy as no flaking of the scale was observed in the ceramic crucible after the experiment or during handling.

Between approximately 10  $\mu\text{m}$  and 40  $\mu\text{m}$  of Fig. 10, the copper content steadily decreases as the nickel content steadily increases. With the Fe and O content in the region remaining fixed, one can assume a substitution of nickel for copper in the ferrite structure with



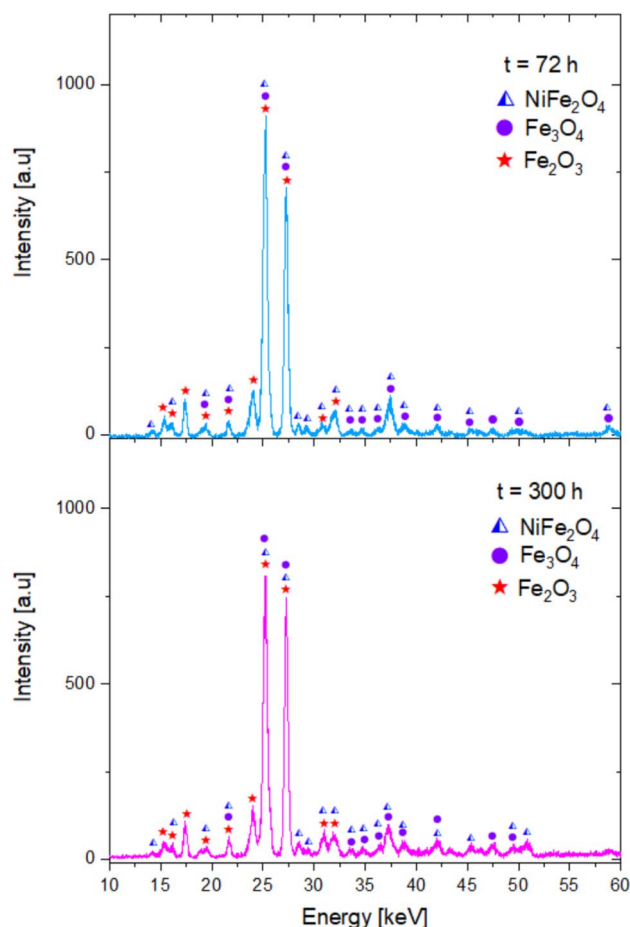
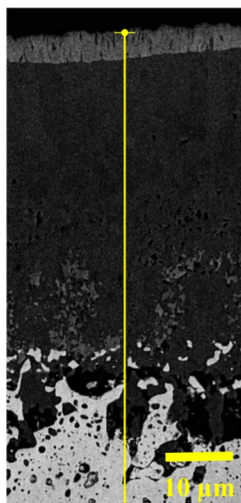


**Figure 9** Energy-dispersive XRD spectra of homogeneous  $\text{Ni}_{42}\text{Fe}_{38}\text{Cu}_{20}$  wt.% oxidised for 72 h and 300 h in 1 atm of  $\text{O}_2$  at 800 °C. Overlapping reflections due to similar lattice parameters between  $\text{NiFe}_2\text{O}_4$ ,  $\text{Fe}_2\text{O}_3$  and  $\text{Fe}_3\text{O}_4$  somewhat obfuscates peak identification.

**Figure 10** Line scan of a cross section of homogeneous  $\text{Ni}_{42}\text{Fe}_{38}\text{Cu}_{20}$  wt.% oxidised in 1 atm of  $\text{O}_2$  at 800 °C for 300 h. The non-repeating pattern is displayed. The system is dominated by the growth of the  $\text{NiFe}_2\text{O}_4$  region. Oxidation at this stage appears relatively uniform. The copper and nickel enrichment of the alloy at the alloy–oxide interface is also clearly displayed.



nickel becoming dominant at a depth of approximately 30  $\mu\text{m}$ . The thickness increase of both ferrite layers as well as the  $\text{CuO}$  layer was all observed with SEM/EDX analysis, with the potential  $\text{CuFe}_2\text{O}_4$  layer in the 5 h cross section being too thin to clearly distinguish.

Figure 10 shows the oxide layer roughly split into different zones:

I: An external  $\text{CuO}$  layer due to the outward diffusion of copper.

II: A predominantly  $\text{CuFe}_2\text{O}_4$  region steadily decreasing in concentration away from the external  $\text{CuO}$  layer as  $\text{NiFe}_2\text{O}_4$  concentration increases. Mixed  $(\text{Cu},\text{Ni})\text{Fe}_2\text{O}_4$  may also form here. Constituent  $\text{Fe}_2\text{O}_3$  oxides exist in this region, fuelling continued copper and nickel spinel growth.

III: Predominantly  $\text{NiFe}_2\text{O}_4$  layer.  $\text{NiO}$  and  $\text{Fe}_2\text{O}_3$ , constituent oxides yet to be consumed, exist in greater concentration near the alloy–oxide interface.

IV: Deep-laying  $\text{Fe}_3\text{O}_4$  (corresponds to approx. 70% Fe which matches the line scan data well when accounting for some nickel) sub-layer with  $\text{NiO}$  as well as fresh unoxidised metal.

V: Depletion zone enriched in nickel and copper and lacking in iron. Approximately 40–50  $\mu\text{m}$  in depth until bulk alloy  $\text{Ni-Fe}$  and  $\text{Cu}$  amounts resume.

EDX analysis reveals two typical morphologies that are observed. The first is as shown in Figs. 5 and 10, the second in Fig. 11. The first can be adequately described from the existing understanding of the

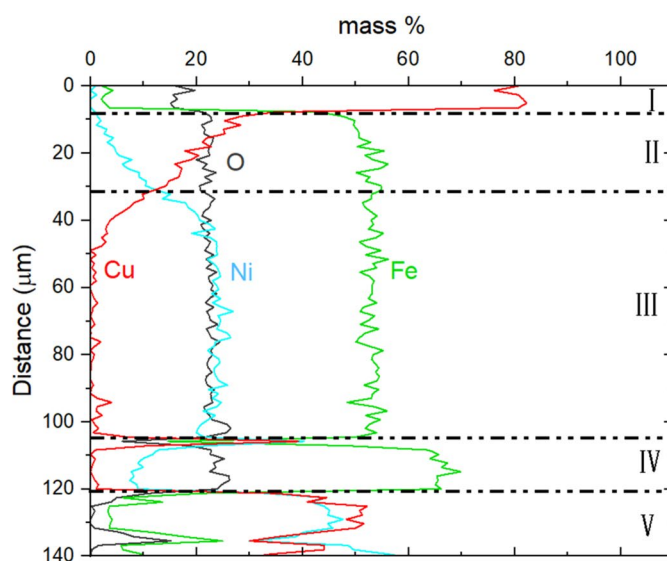
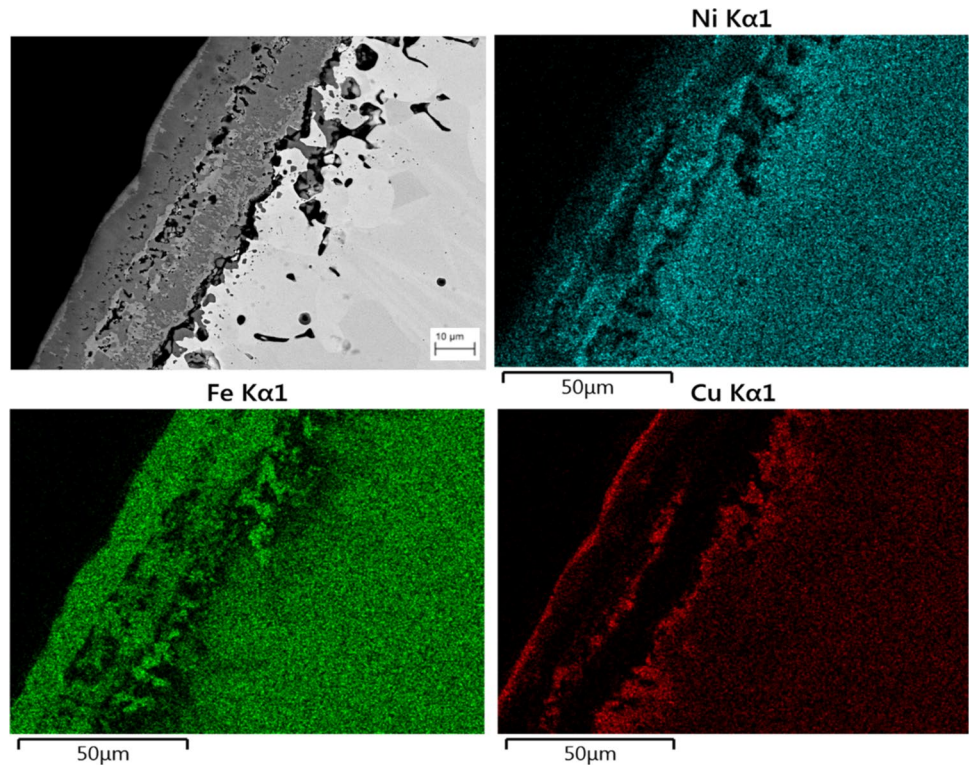


**Figure 11** SEM image of homogenised  $\text{Ni}_{42}\text{Fe}_{38}\text{Cu}_{20}$  wt.% oxidised under 1 atm of  $\text{O}_2$  at 800 °C for 18 h. EDX map shows the distribution of nickel (top right), iron (bottom left) and copper (bottom right) within the oxide scale.



kinetics and thermodynamics of the constituent metals. Initial iron oxide formations are thermodynamically favoured and partition the copper and nickel out of its structure. Copper, with the highest diffusion coefficient (then iron and nickel, respectively), diffuses outwards to the surface of the alloy where it meets fresh oxygen. The increased copper concentration on the surface means the formation of  $\text{CuO}$  dominates the initial oxidation rate. Within this system, oxide scales are typically characterised by an external  $\text{Cu}_x\text{O}$  ( $x = 1, 2$ ) layer [27]. Oxygen diffusion through the external  $\text{CuO}$  layer persists and a layer of iron oxides ( $\text{FeO}$ ,  $\text{Fe}_2\text{O}_3$ ,  $\text{Fe}_3\text{O}_4$ ) preferentially grows. No evidence of  $\text{FeO}$  was found with XRD or EDX analysis, suggesting it readily oxidises further. Nickel atoms may be dispersed within this iron layer as a solid solution which oxidises to form  $\text{NiO}$ . The relative immobility of nickel atoms [17, 27] as well as the depletion of iron immediately beneath the scale at the oxide–alloy interface leads to greater internal  $\text{NiO}$  phase formation close to the oxide–alloy interface. The spinel oxides  $\text{CuFe}_2\text{O}_4$  and  $\text{NiFe}_2\text{O}_4$  are able to form in regions where the simple oxides lay in proximity. For copper ferrite,  $\text{CuO} + \text{Fe}_2\text{O}_3 \rightarrow \text{CuFe}_2\text{O}_4$  and  $\text{NiO} + \text{Fe}_2\text{O}_3 \rightarrow \text{NiFe}_2\text{O}_4$  for nickel ferrite, respectively. Deep-laying  $\text{Fe}_3\text{O}_4$  is not observed in significant amounts, evolving to  $\text{Fe}_2\text{O}_3$  and

allowing for the ferrite-forming reactions. A predominantly nickel ferrite scale is already observed after 5 h suggesting the simple iron oxides are relatively unstable in the presence of enough  $\text{NiO}$ .

Figure 5 shows how the constituent metals orientate themselves in this alloy during oxidation via EDX mapping. The outer  $\text{CuO}$  layer is clearly visible and a sub-layer of copper which clearly overlaps with a strong concentration of iron suggests to presence of copper ferrite. Similarly, there are clear overlapping regions of nickel and iron in the oxide scale in uniform amounts that suggest the formation of nickel ferrite. The presence of both of these ferrite regions increases in both width and density over time, most prominent after 300 h of oxidation.

Figure 11 shows the second typical morphology of the scale, more noticeable in the 5-h, 8-h and 18-h oxidation measurements where the rate of oxidation is more rapid. Partial separation of the scale occurs, locally affecting the diffusion of cations and anions.  $\text{CuO}$  and  $\text{NiO}$  are present in incoherent layers around a crack in the middle of the scale, the rest of the oxide scale taking the typical structure as from Figs. 5 and 10.

In both cases the scale is dominated by iron-based oxides ( $\text{Fe}_2\text{O}_3$ ,  $\text{Fe}_3\text{O}_4$ ,  $\text{NiFe}_2\text{O}_4$ ) due to its high

driving force of oxidation, with partial scale detachment promoting the formation of CuO and NiO moresos. The copper sub-layer indicative of  $\text{CuFe}_2\text{O}_4$  is visible in both 8-h (not shown) and 18-h oxidised samples but becomes difficult to distinguish in the 5-h sample via EDX. This at least suggests after, at most, 8 h both ferrite compounds are present in the scale. A depletion zone of iron beneath the oxide–alloy interface that grows proportionally over time is always observed, alongside a subsequent copper and nickel enrichment.

In Fig. 11 the scale can be broadly seen to be split into two regions, due to a partial separation of the scale. Initial oxide formation broadly follows the typical process as previously described. A crack forms, behind which the inner scale oxidises semi-independently from the scale above. Uneven oxidation due to cracks or surface imperfections is observed as pockets of untouched alloy—enriched in nickel and copper as per Fig. 12—are visible. A similar, generalised mechanism is described in Wood et al. [28]. Continued outward diffusion of copper to the oxide surface is blocked by the porosity and accumulates to form an incoherent CuO layer, as well as increased NiO due to relative nickel enrichment. The inner CuO layer appears to be able to seed further  $\text{CuFe}_2\text{O}_4$  formation, suggesting the availability of copper is the limiting factor for this phase. For the 5-h, 8-h and 18-h series of measurements the partially detached regions are larger relative to the scale compared to 72-h and 300-h runs.

At longer times relative oxides surrounding porosities become less prevalent and the scale contains less CuO/NiO. Images of the 72-h sample show non-uniform internal oxidation at the alloy–oxide interface and the formation of copper and nickel-rich “islands” as well as mostly iron-based oxides rather than CuO/NiO. Similarly for the 300-h sample, CuO and NiO oxides are less prevalent in the bulk of the scale. CuO and NiO oxides that form in the initial stages of oxidation, are not visible throughout the entirety of the scale and must therefore react with  $\text{Fe}_2\text{O}_3$  producing (Cu/Ni, Fe)O spinel oxides. CuO and NiO oxides are more prevalent in the bulk oxide at parabolic oxidation rates, where partial scale separation appears more common, diminishing over time as the alloy transitions into cubic rate behaviour and internal mechanical stresses due to oxide growth weaken. Over enough time, the partially detached regions of the scale with their different oxide morphologies evolve to the

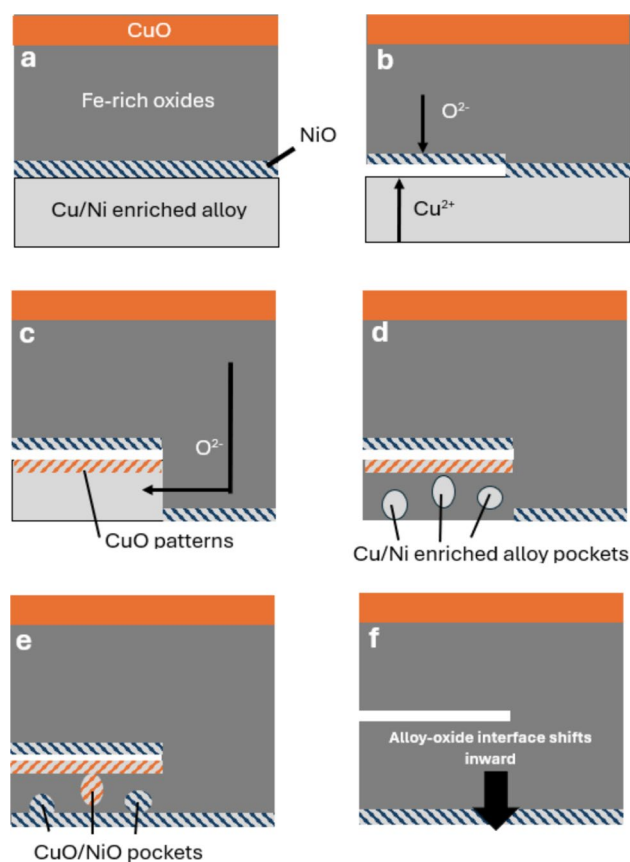


**Figure 12** Schematic diagram of proposed mechanism about how a large enough cracks affect local kinetics of the oxidation process in homogenised  $\text{Ni}_{42}\text{Fe}_{38}\text{Cu}_{20}$  wt.% at  $800^\circ\text{C}$  under 1 atm of  $\text{O}_2$ , from left to right. Starting with the typical structure (a), a crack in the oxide scale forms at the alloy–oxide interface (b), impeding local diffusion of oxygen and copper and partially isolating the iron-depleted alloy from the scale. Incoherent CuO and NiO patterns lay below and above the crack, respectively. Oxygen diffusion around the porosity is impeded—due to a reduced cross-sectional area—into the copper–nickel-enriched alloy, (c). This causes copper–nickel-rich alloy “islands” to form as the region behind the crack oxidises non-uniformly (d), oxidation of iron still dominates. More incoherent patterns of CuO and NiO form in the region behind the crack (e). Over longer timescales, these oxides react to form spinel (Cu/Ni, Fe) O oxides and diffuse into the iron-based sub-scale as oxidation continues (f).

uniform structure shown in Fig. 10. Locally affected oxide structures due to partial detachment are therefore only temporary, and the scale can be seen to self-repair.



## Conclusion

The oxidation behaviour of single FCC phase  $\text{Ni}_{29}\text{Fe}_{56}\text{Cu}_{15}$  wt.%,  $\text{Ni}_{60}\text{Fe}_{30}\text{Cu}_{10}$  wt.% and  $\text{Ni}_{42}\text{Fe}_{38}\text{Cu}_{20}$  wt.% was studied via TGA with 1 atm of  $\text{O}_2$  at 800 °C as a function of exposure time for 18 h. All alloys were observed to form an Fe-rich oxide scale and follow a parabolic rate behaviour. XRD and EDX analysis confirmed the presence of CuO,  $\text{Fe}_2\text{O}_3$ ,  $\text{NiFe}_2\text{O}_4$  and NiO phases. Coarse spinodal decomposition was observed in the bulk of the least Ni-rich alloy,  $\text{Ni}_{29}\text{Fe}_{56}\text{Cu}_{15}$  wt.%—an indicator of poor performance during electrolysis for this system [8].

Further oxidation tests under the same oxidising conditions of the two thermodynamically stable alloys,  $\text{Ni}_{60}\text{Fe}_{30}\text{Cu}_{10}$  wt.% and  $\text{Ni}_{42}\text{Fe}_{38}\text{Cu}_{20}$  wt.%, ensued for isothermal holding times of 272 h and 300 h, respectively. Approximately cubic rate behaviour—yet to be documented up until this present study in this ternary system—was achieved for both alloys. The  $\text{Ni}_{42}\text{Fe}_{38}\text{Cu}_{20}$  wt.% alloy exhibited cubic behaviour after 30 h up until 300 h with no catastrophic breakaway oxidation occurring. EDX analysis revealed the presence of a compact  $\text{NiFe}_2\text{O}_4$  dominated scale with good adhesion to the bulk. In contrast,  $\text{Ni}_{60}\text{Fe}_{30}\text{Cu}_{10}$  wt.% was observed to enter a cubic regime for only the last 8 h of its 272-h isothermal run-time, with local regions of extensive oxidation occurring due to poor scale adhesion followed by intergranular corrosion penetrating the bulk up to >0.5 mm. Furthermore, oxidation of  $\text{Ni}_{60}\text{Fe}_{30}\text{Cu}_{10}$  wt.% over time appeared to lend itself to an increasing proportion of NiO in the oxide scale, rather than a more favourable spinel (Ni, Fe)O region.

The strong presence of a compact  $\text{NiFe}_2\text{O}_4$  scale in  $\text{Ni}_{42}\text{Fe}_{38}\text{Cu}_{20}$  wt.% correlates with the promising electrolytic performance of this alloy [9] due to the chemical stability of the oxide in molten salt solutions [4, 5], with this study presenting an alloy design that appears to maximise nickel ferrite formation at 800 °C in the presence of  $\text{O}_2$  over long exposure times. After 300 h of oxidation, very little  $\text{Fe}_2\text{O}_3$  and NiO were observed suggesting the Ni:Fe ratio in particular appears to be close to optimal for forming  $\text{NiFe}_2\text{O}_4$  phase. Optimisation of the Ni:Fe ratio to further maximise the formation of  $\text{NiFe}_2\text{O}_4$  is left open for further investigation. The existence of a growing  $\text{CuFe}_2\text{O}_4$  phase below the CuO layer was observed in  $\text{Ni}_{42}\text{Fe}_{38}\text{Cu}_{20}$  wt.%, likely due to continued outward diffusion of copper during oxidation causing a local enrichment of copper, subsequently

reacting with constituent  $\text{Fe}_2\text{O}_3$ . The copper enrichment underneath the CuO appears to give rise to a (Cu,Ni) $\text{Fe}_2\text{O}_4$  phase with copper being substituted out for nickel with increasing depth as per Fig. 10, although XRD analysis was inconclusive in this regard and further investigations are required.

The oxidation mechanism behind this particular scale formation was investigated with five separate oxidation experiments with isothermals lasting 5 h, 8 h, 18 h, 72 h and 300 h under the same oxidising conditions as previously mentioned. A distinct oxide structure was observed, in particular at 5–18 h, where partial separation of the scale (likely due to greater growth stresses during the more rapid initial oxidation) appears to locally disrupt the formation of the  $\text{NiFe}_2\text{O}_4$  phase. Instead, CuO and NiO form in greater quantities due to nickel and copper enrichment directly beneath the scale. The disruption of oxide kinetics caused by local separation of the scale has been documented in other systems, [29–32]. Local changes to oxide formation around these partially detached regions were shown to be much more drastic at lower oxidation times, where the size of the cracks was large relative to the size of the scale and the oxidation rate was higher. CuO and NiO tended to form in proximity to porosities that lay in the bulk of the scale, in regions where they were otherwise observed *not* to consistently form. At longer times these oxides diffuse into the scale forming (Cu/Ni, Fe)O spinel oxides.

Partially detached regions of the scale may allow for bath penetration in regions with a higher proportion of CuO and NiO rather than the more insoluble  $\text{NiFe}_2\text{O}_4$  phase. Reduced internal growth strains in the scale via a slower heating protocol or changing of the alloy design while approximately preserving the Ni:Fe ratio may help to form an even more compact,  $\text{NiFe}_2\text{O}_4$  dominated scale.

## Acknowledgements

This work is dedicated to the memory of Michael E. Kassner, in recognition of his pioneering approach to sustainable metallurgy. Around 25 years ago, he had the foresight to initiate this research into developing metallic inert anodes for aluminium production as part of a Oregon Metals Initiative grant. The authors would like to thank P. Polcik, D. Cox, M. Stemmler, A. Manzoni and R. Saliwan for technical support.

## Author contributions

T. Jamieson performed a majority of the experimental investigation excluding XRD, a majority of the analysis and interpretation, wrote the majority of the manuscript and conceptualised the study. D. Apel performed all of the XRD experiments and a majority of the analysis with input from T. Jamieson and contributed to writing the manuscript. Andrey Yasinskiy assisted in the review and editing of the manuscript as well as conceptualisation. Roman Düssel assisted in the review and editing, project administration and funding acquisition. P. Decker assisted in the conceptualisation of the study, review and editing and XRD data interpretation. G. Gunnarsson assisted in the review and editing. K. Singh assisted in the review and editing as well as conceptualisation. J. Magnusson assisted in funding acquisition. B. Adam assisted in the review and editing as well as experimental investigation. R. Busch assisted in the supervision and resource allocation of this study. B. Friedrich assisted in supervision. I. Gallino contributed to the conceptualisation, review and editing, supervision, resource allocation and funding acquisition of this study.

## Funding

Open Access funding enabled and organized by Projekt DEAL. The authors acknowledge funding through the Progres.NRW programme (EFRE.NRW) for the project “CO<sub>2</sub>-free Aluminium Production”.

## Data availability

Data used during the current study can be made available from the corresponding author on request.

## Code availability

N/A.

## Materials availability

Data used during the current study can be made available from the corresponding author on request.

## Declarations

**Conflict of interest** The authors declare no conflict of interest.

**Ethics approval and consent to participate** N/A.

**Consent for publication** N/A.

**Open Access** This article is licensed under a Creative Commons Attribution 4.0 International License, which permits use, sharing, adaptation, distribution and reproduction in any medium or format, as long as you give appropriate credit to the original author(s) and the source, provide a link to the Creative Commons licence, and indicate if changes were made. The images or other third party material in this article are included in the article's Creative Commons licence, unless indicated otherwise in a credit line to the material. If material is not included in the article's Creative Commons licence and your intended use is not permitted by statutory regulation or exceeds the permitted use, you will need to obtain permission directly from the copyright holder. To view a copy of this licence, visit <http://creativecommons.org/licenses/by/4.0/>.

## References

- [1] Primary Aluminium Production (2024). <https://international-aluminium.org/statistics/primary-aluminium-production>. Accessed 16 May 2024
- [2] Beck TR, Brooks RJ (1989) Electrolytic reduction of alumina. US. Patent 4,865,701 12:75–174
- [3] Beck TR (1995) A non-consumable metal anode for production of aluminum with low-temperature fluoride melts. *Light Met* 69:355–360
- [4] Beck TR, Macrae CM, Wilson NC (2011) Metal anode performance in low-temperature electrolytes for aluminum production. *Metall Mater Trans B* 42:807–813. <https://doi.org/10.1007/s11663-011-9511-8>
- [5] Galasiu I, Galasiu R, Thonstad J (2007) Inert anodes for aluminium electrolysis, 1st edn. Aluminium-Verlag, Düsseldorf
- [6] Helle S, Pedron M, Assouli B, Davis B, Guay D, Roué L (2010) Structure and high-temperature oxidation behaviour of Cu–Ni–Fe alloys prepared by high-energy ball milling for application as inert anodes in aluminium electrolysis.

- Corros Sci 52(10):3348–3355. <https://doi.org/10.1016/j.corsci.2010.06.011>
- [7] Gavrilo E, Goupil G, Davis B, Guay D, Roué L (2015) On the key role of Cu on the oxidation behavior of Cu–Ni–Fe based anodes for Al electrolysis. Corros Sci 101:105–113. <https://doi.org/10.1016/j.corsci.2015.09.006>
- [8] Gallino I, Curiotto S, Baricco M, Kassner ME, Busch R (2008) Homogenization of highly alloyed Cu–Fe–Ni: a phase diagram study. J Phase Equilib Diffus 29(2):131–135. <https://doi.org/10.1007/s11669-007-9244-1>
- [9] Gallino I (2004) Phase diagram, thermal stability, and high temperature oxidation of the ternary Cu–Ni–Fe system. Ph.D thesis. Oregon State University
- [10] Gallino I, Kassner ME, Busch R (2012) Oxidation and corrosion of highly alloyed Cu–Fe–Ni as inert anode material for aluminum electrowinning in as-cast and homogenized conditions. Corros Sci 63:293–303. <https://doi.org/10.1016/j.corsci.2012.06.013>
- [11] Singh K, Haarberg GM, Mallah AR, Gunnarsson G, Jamieson T, Gallino I, Saevarsdottir G (2024) Overpotential on oxygen-evolving platinum and Ni–Fe–Cu anode for low-temperature molten fluoride electrolytes. JOM 76:3284–3293. <https://doi.org/10.1007/s11837-024-06425-5>
- [12] Yasinskiy A, Jamieson T, Singh K, Gunnarsson G, Magnusson J, Feldhaus D, Düssel R, Gallino I, Friedrich B (2024) Correlation between corrosion rate and electrochemical parameters of anode process on the metallic electrode in molten oxyfluorides. Light Met 596–601
- [13] Padamata SK, Singh K, Haarberg GM, Saevarsdottir G (2024) Anodic behavior of Ni<sub>48</sub>Fe<sub>47</sub>Cu<sub>5</sub> and Ni<sub>42</sub>Fe<sub>38</sub>Cu<sub>20</sub> in potassium-rich NaF–KF–AlF<sub>3</sub>–Al<sub>2</sub>O<sub>3</sub> melts. JOM 76:3275–3283. <https://doi.org/10.1007/s11837-024-06512-7>
- [14] Saevarsdottir G, Haarberg GM, Bourmaud M, Singh K, Padamata SK (2023) Anodic behaviour of Ni<sub>42</sub>Fe<sub>38</sub>Cu<sub>20</sub> electrode in molten fluoride salts. Electrochem Soc 170:072508. <https://doi.org/10.1149/1945-7111/ace5e3>
- [15] Ying L, Dengpeng C, Wei W, Dongsheng L, Junwei W, Yudong L, Zhirong S (2020) Influences of heat treatment on the oxidation and corrosion behavior of Cu–Ni–Fe inert anodes for aluminium electrolysis. J Alloy Compd 832:154848. <https://doi.org/10.1016/j.jallcom.2020.154848>
- [16] Jucken S, Schaal E, Tougas B, Davis B, Guay D, Roué L (2019) Impact of a post-casting homogenization treatment on the high-temperature oxidation resistance of a Cu–Ni–Fe alloy. Corros Sci 147:321–329. <https://doi.org/10.1016/j.corsci.2018.11.037>
- [17] Haugsrud R, Norby T, Kofstad P (2001) High-temperature oxidation of Cu–30 wt.% Ni–15 wt.% Fe. Corros Sci 43:283–299. [https://doi.org/10.1016/S0010-938X\(00\)00080-9](https://doi.org/10.1016/S0010-938X(00)00080-9)
- [18] Niu Y, Gesmundo F (2001) Oxidation of a ternary Cu–Ni–Fe alloy under low oxygen pressures at 800–900 °C. J Alloys Compd 317–318:578–582. [https://doi.org/10.1016/S0925-8388\(00\)01391-8](https://doi.org/10.1016/S0925-8388(00)01391-8)
- [19] Helle S, Brodu B, Davis B, Guay D, Roué L (2011) Influence of the iron content in Cu–Ni based inert anodes on their corrosion resistance for aluminium electrolysis. Corros Sci 53:3248–3253. <https://doi.org/10.1016/j.corsci.2011.05.069>
- [20] Atkins P, Paula J (2006) Physical chemistry: thermodynamics and kinetics, 8th edn. Oxford University Press, Oxford, p 215
- [21] Cappell B, Was G (2007) Selective internal oxidation as a mechanism for intergranular stress corrosion cracking of Ni–Cr–Fe alloys. Metall Mater Trans A 38:1244–1259. <https://doi.org/10.1007/s11661-007-9124-7>
- [22] Parkins RN (1995) Mechanistic aspects of the intergranular stress corrosion cracking of ferritic steels. In: Proceedings of the corrosion, pp 1–20. <https://doi.org/10.5006/C1995-95183>
- [23] Zhang S, Liu X, Wang W, Han E, Kuang W (2024) On the stress corrosion crack initiation behaviour of alloy 800 in high-temperature hydrogenated water. Corros Sci 238:112358. <https://doi.org/10.1016/j.corsci.2024.112358>
- [24] Kenfack F, Langbein H (2006) Spinel ferrites of the quaternary system Cu–Ni–Fe–O: Synthesis and characterization. J Mater Sci 41:3683–3693. <https://doi.org/10.1007/s10853-006-6263-y>
- [25] Manju BG, Raji P (2019) Green synthesis of nickel–copper mixed ferrite nanoparticles: structural, optical, magnetic, electrochemical and antibacterial studies. J Electron Mater 48:7710–7720. <https://doi.org/10.1007/s11664-019-07603-x>
- [26] Nihore A, Aziz F, Oswal N, Jain P, Subodhi O, Gupta N (2019) Synthesis and characterization of copper doped nickel ferrite prepared by sol–gel method. Mater Today Proc 18:3651–3656. <https://doi.org/10.1016/j.matpr.2019.07.298>
- [27] Divinski SV, Hisker F, Herzig C, Filippek R, Danielewski M (2005) Self and interdiffusion in ternary Cu–Fe–Ni alloys. Defect Diffus Forum 237–240:50–61. <https://doi.org/10.4028/www.scientific.net/DDF.237-240.50>
- [28] Wood GC, Stott FH (1987) Oxidation of alloys. Mater Sci Technol 3(7):519–530. <https://doi.org/10.1016/j.corsci.2019.108234>
- [29] Persdotter A, Sattari M, Larsson E, Ogaz MAO, Liske J, Jonsson T (2020) Oxidation of Fe–2.25Cr–1Mo in presence of KCl(s) at 400 °C – crack formation and its influence on oxidation kinetics. Corros Sci 163:108234. <https://doi.org/10.1016/j.corsci.2019.108234>



- [30] Wen J, Cao R, Che H, Dong H, Zhang H, Yan Y, Gao Y, Liaw PK (2020) The oxidation effect on the cracking behavior of a Co-based alloy under thermal shocks. *Corros Sci* 173:108828. <https://doi.org/10.1016/j.corsci.2020.108828>
- [31] Viskari L, Hoernqvist M, Moore KL, Cao Y, Stiller K (2013) Intergranular crack tip oxidation in a Ni-base superalloy. *Acta Mater* 61:3629–3630. <https://doi.org/10.1016/j.actamat.2013.02.050>
- [32] Behnamian Y, Mostafei A, Kohandehghan A, Amirkhiz BS, Li J, Zheng W, Guzonas D, Chmielus M, Chen W, Luo JL (2017) Characterization of oxide layer and micro-crack initiation in alloy 316L stainless steel after 20,000 h exposure to supercritical water at 500°C. *Mater Charact* 131:532–543. <https://doi.org/10.1016/j.matchar.2017.07.029>

**Publisher's Note** Springer Nature remains neutral with regard to jurisdictional claims in published maps and institutional affiliations.

## Terms and Conditions

Springer Nature journal content, brought to you courtesy of Springer Nature Customer Service Center GmbH (“Springer Nature”).

Springer Nature supports a reasonable amount of sharing of research papers by authors, subscribers and authorised users (“Users”), for small-scale personal, non-commercial use provided that all copyright, trade and service marks and other proprietary notices are maintained. By accessing, sharing, receiving or otherwise using the Springer Nature journal content you agree to these terms of use (“Terms”). For these purposes, Springer Nature considers academic use (by researchers and students) to be non-commercial.

These Terms are supplementary and will apply in addition to any applicable website terms and conditions, a relevant site licence or a personal subscription. These Terms will prevail over any conflict or ambiguity with regards to the relevant terms, a site licence or a personal subscription (to the extent of the conflict or ambiguity only). For Creative Commons-licensed articles, the terms of the Creative Commons license used will apply.

We collect and use personal data to provide access to the Springer Nature journal content. We may also use these personal data internally within ResearchGate and Springer Nature and as agreed share it, in an anonymised way, for purposes of tracking, analysis and reporting. We will not otherwise disclose your personal data outside the ResearchGate or the Springer Nature group of companies unless we have your permission as detailed in the Privacy Policy.

While Users may use the Springer Nature journal content for small scale, personal non-commercial use, it is important to note that Users may not:

1. use such content for the purpose of providing other users with access on a regular or large scale basis or as a means to circumvent access control;
2. use such content where to do so would be considered a criminal or statutory offence in any jurisdiction, or gives rise to civil liability, or is otherwise unlawful;
3. falsely or misleadingly imply or suggest endorsement, approval, sponsorship, or association unless explicitly agreed to by Springer Nature in writing;
4. use bots or other automated methods to access the content or redirect messages
5. override any security feature or exclusionary protocol; or
6. share the content in order to create substitute for Springer Nature products or services or a systematic database of Springer Nature journal content.

In line with the restriction against commercial use, Springer Nature does not permit the creation of a product or service that creates revenue, royalties, rent or income from our content or its inclusion as part of a paid for service or for other commercial gain. Springer Nature journal content cannot be used for inter-library loans and librarians may not upload Springer Nature journal content on a large scale into their, or any other, institutional repository.

These terms of use are reviewed regularly and may be amended at any time. Springer Nature is not obligated to publish any information or content on this website and may remove it or features or functionality at our sole discretion, at any time with or without notice. Springer Nature may revoke this licence to you at any time and remove access to any copies of the Springer Nature journal content which have been saved.

To the fullest extent permitted by law, Springer Nature makes no warranties, representations or guarantees to Users, either express or implied with respect to the Springer nature journal content and all parties disclaim and waive any implied warranties or warranties imposed by law, including merchantability or fitness for any particular purpose.

Please note that these rights do not automatically extend to content, data or other material published by Springer Nature that may be licensed from third parties.

If you would like to use or distribute our Springer Nature journal content to a wider audience or on a regular basis or in any other manner not expressly permitted by these Terms, please contact Springer Nature at

[onlineservice@springernature.com](mailto:onlineservice@springernature.com)